

Data-Efficient Multidimensional Free Energy Estimation via Physics-Informed Score Learning

Daniel Nagel^{1, a)} and Tristan Bereau^{1, 2}

¹⁾ Institute for Theoretical Physics, Heidelberg University, 69120 Heidelberg, Germany

²⁾ Interdisciplinary Center for Scientific Computing (IWR), Heidelberg University, 69120 Heidelberg, Germany

(Dated: 12 February 2026)

Many biological processes involve numerous coupled degrees of freedom, yet free-energy estimation is often restricted to one-dimensional profiles to mitigate the high computational cost of multidimensional sampling. In this work, we extend Fokker–Planck Score Learning (FPSL) to efficiently reconstruct two-dimensional free-energy landscapes from non-equilibrium molecular dynamics simulations using different types of collective variables. We show that explicitly modeling orthogonal degrees of freedom reveals insights hidden in one-dimensional projections at negligible computational overhead. Additionally, exploiting symmetries in the underlying landscape enhances reconstruction accuracy, while regularization techniques ensure numerical robustness in sparsely sampled regions. We validate our approach on three distinct systems: the conformational dynamics of alanine dipeptide, as well as coarse-grained and all-atom models of solute permeation through lipid bilayers. We demonstrate that, because FPSL learns a smooth score function rather than histogram-based densities, it overcomes the exponential scaling of grid-based methods, establishing it as a data-efficient and scalable tool for multidimensional free-energy estimation.

I. INTRODUCTION

Free-energy landscapes provide the thermodynamic map for molecular processes, describing the stability of states and the kinetics of transitions between them.^{1–3} While these landscapes are inherently high-dimensional, defining them is typically done by projecting the complex configurational space onto a small set of collective variables (CVs). In practice, this projection is often restricted to a single dimension to minimize computational cost. However, this reduction relies on the strong assumption that all orthogonal degrees of freedom equilibrate rapidly. When this timescale separation fails, one-dimensional profiles suffer from hysteresis, hidden barriers, and systematic errors.⁴ Extending the analysis to two dimensions is often necessary to resolve these artifacts, yet robustly estimating two-dimensional (2D) free-energy surfaces remains a significant computational bottleneck.

Equilibrium sampling approaches remain foundational for free-energy calculations. Metadynamics adaptively deposits history-dependent bias to escape deep minima,⁵ adaptive biasing force (ABF) methods apply on-the-fly forces to flatten barriers,⁶ while other methods, such as replica-exchange⁷ and accelerated molecular dynamics,⁸ can further enhance sampling efficiency. Nevertheless, umbrella sampling–based methods remain the current gold standard: by applying overlapping harmonic restraints, umbrella sampling^{9,10} ensures comprehensive coverage of high-energy regions, and the weighted histogram analysis method (WHAM)^{11,12} or multistate Bennett acceptance ratio (MBAR)¹³ estimators reconstruct the unbiased potential of mean force (PMF) from

the biased samples. These methods have become a workhorse for various biomolecular applications, ranging from protein-ligand binding^{14–16} to solute permeation through lipid bilayers.^{17–22} However, these conventional methods face a steep trade-off between accuracy and scaling. Grid-based approaches like umbrella sampling suffer from the “curse of dimensionality” starting from 2D, where the number of overlapping windows required to cover the grid grows exponentially. Conversely, non-equilibrium methods based on Jarzynski’s equality²³ theoretically apply to any dimension but struggle to converge when work distributions are broad, limiting their practical utility for complex landscapes.

In this work, we address these limitations by extending the recently introduced *Fokker–Planck Score Learning* (FPSL)²⁴ to multidimensional free-energy estimation. FPSL frames free-energy reconstruction as a generative modeling task, training a diffusion model to learn the equilibrium free-energy landscape from non-equilibrium trajectory data. Crucially, FPSL distinguishes itself by explicitly exploiting the periodicity of the collective variables: it embeds the analytic non-equilibrium steady state (NESS) of a periodic driven system directly into the training objective. This physics-informed prior acts as a powerful inductive bias, allowing one to learn equilibrium free-energy landscapes from non-equilibrium data with high efficiency. For an illustration of the method, see Fig. 1.

Because FPSL is a score-based method, it generalizes readily to higher dimensions without structural changes or significant computational overhead in the learning phase. The neural network simply learns a smooth vector field in a higher-dimensional space. The only added complexity lies in the physical sampling: higher-dimensional spaces naturally require longer molecular dynamics (MD) simulations to sufficiently sample the NESS distribution.

^{a)} Electronic mail: nagel.phys@gmail.com

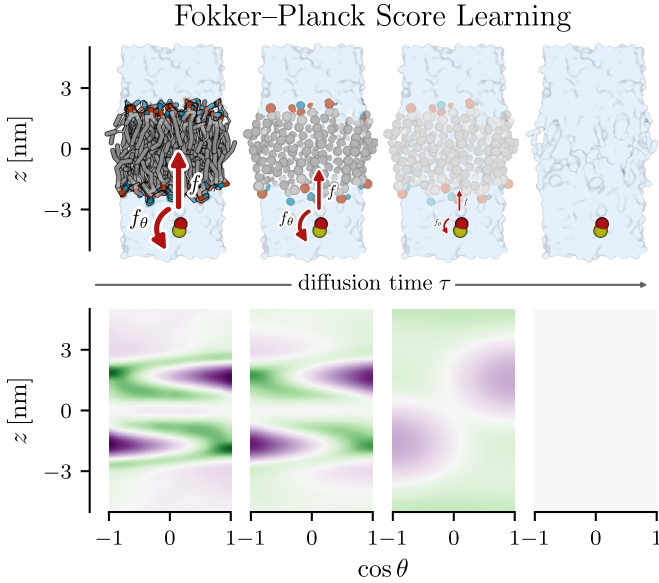


FIG. 1. We consider a system with periodic boundary conditions, characterized by a conservative potential of mean force, $U(z, \theta)$. The center of mass of the composite particle (red and yellow) is driven by a constant external force f , while its orientation is subject to a constant torque f_θ . The steady-state solution of the Fokker-Planck equation for a Brownian particle in a periodic potential, p^{ss} , informs the score of our diffusion model, mapping the non-equilibrium steady state to the equilibrium distribution. The diffusion model smoothly interpolates between the physical non-equilibrium system at constant flux J (left) and a trivial uniform prior (right). Denoising allows us to efficiently reconstruct the two-dimensional equilibrium free-energy landscape (bottom row) by exploiting the structure of p^{ss} .

However, we show that this investment is highly efficient. We demonstrate that even when the primary interest lies in a one-dimensional profile, it is advantageous to learn the full 2D landscape and subsequently marginalize over the orthogonal degree of freedom. This approach resolves hidden barriers and yields faster convergence than direct 1D estimation or conventional umbrella sampling-based MBAR.

We validate the versatility of this framework by applying it to three distinct systems: the conformational dynamics of alanine dipeptide in water, described by two dihedral angles; the permeation of a solute through a lipid bilayer modeled with a coarse-grained force field, which introduces a non-periodic orientational degree of freedom alongside a periodic spatial coordinate; and the permeation of ethanol through a membrane modeled in all-atom detail. These applications highlight the generality of FPSL: the method is agnostic to the nature of the collective variables—whether Cartesian coordinates such as the position within the simulation box or internal coordinates such as dihedral angles—and to the force field resolution. Because FPSL relies solely on the ability to efficiently sample the stationary probability density in the CV space, which is naturally facilitated by

the periodicity of the driving coordinate, it requires no system-specific adaptations. This provides a unified and efficient route to multidimensional free-energy estimation of collective variables that can be mapped to periodic domains.

The remainder of this paper is organized as follows. Sec. II recalls the derivation of Fokker-Planck Score Learning and details its extension to 2D systems, including the enforcement of symmetries and the use of Fokker-Planck regularization. Sec. III presents the results for the three test cases, demonstrating the superior convergence and accuracy of our 2D approach compared to standard baselines. Finally, we summarize our findings in Sec. IV.

II. THEORY AND METHODS

A. Background

We briefly review the theoretical foundations of score-based diffusion models and the non-equilibrium steady state (NESS) for periodic systems, which together form the basis of Fokker-Planck Score Learning (FPSL).²⁴ For comprehensive derivations, we refer to Song et al.²⁵ and Risken.²⁶

Score-Based Diffusion Models on Periodic Domains: Denoising diffusion models (DDMs) reconstruct a target distribution $p_{\text{data}}(x)$ by inverting a gradual noising process.^{25,27,28} On a periodic domain of size L , the forward process is a Brownian motion on the torus,

$$dx_\tau = \sqrt{2\alpha_\tau} dW_\tau, \quad (1)$$

where $\tau \in [0, 1]$ is the dimensionless diffusion time and $\alpha_\tau > 0$ the noise schedule. As $\tau \rightarrow 1$, the distribution relaxes to a uniform prior over $[-L/2, L/2]$. The corresponding reverse-time SDE²⁹

$$dx_\tau = -2\alpha_\tau \nabla \ln p_\tau(x_\tau) d\tau + \sqrt{2\alpha_\tau} d\bar{W}_\tau, \quad (2)$$

maps the uniform prior back to the data distribution, with the score function $s(x_\tau, \tau) = \nabla \ln p_\tau(x_\tau)$ governing the drift.

The score is learned via denoising score matching.²⁵ Noised samples $x_\tau = x_0 + \sigma_\tau \varepsilon$, with $\varepsilon \sim \mathcal{N}(0, 1)$ and $\tau \sim \mathcal{U}([0, 1])$, are wrapped onto the periodic domain, and a neural network $\varepsilon_\theta(x_\tau, \tau)$ is trained to predict the added noise by minimizing

$$\mathcal{L}_{\text{DSM}}(\theta) = \mathbb{E}_{x_0 \sim p_0, \varepsilon, \tau} \left[\|\varepsilon_\theta(x_\tau, \tau) - \varepsilon\|^2 \right], \quad (3)$$

where the relationship $s_\theta(x_\tau, \tau) = -\varepsilon_\theta(x_\tau, \tau)/\sigma_\tau$ recovers the score from the predicted noise. To ensure that the learned score corresponds to the gradient of a scalar potential, we employ energy-based diffusion models,^{30–32} parameterizing the noise as

$$\frac{\varepsilon_\theta(x_\tau, \tau)}{\sigma_\tau} = -s_\theta(x_\tau, \tau) = \beta \nabla U_\theta(x_\tau, \tau), \quad (4)$$

where U_θ is a learnable, time-dependent potential energy function (in units of $k_B T$) and $\beta = (k_B T)^{-1}$. The gradient is computed via automatic differentiation.

Non-Equilibrium Steady State of a Periodic System: Consider a particle undergoing overdamped Langevin dynamics in a periodic potential $U(x)$ subject to a constant external force f . Defining the effective (tilted) potential $U_{\text{eff}}(x) = U(x) - fx$, the corresponding Fokker–Planck equation admits a time-independent solution with constant probability current.²⁶ Specifically, the probability density $p_t(x)$ evolves according to

$$\begin{aligned}\partial_t p_t(x) &= \nabla \{ \beta D \nabla U_{\text{eff}}(x) p_t(x) \} + D \nabla^2 p_t(x) \\ &= -\nabla J_t(x),\end{aligned}\quad (5)$$

where D is the diffusion coefficient and $J_t(x)$ is the probability current. In the steady-state limit, the current becomes spatially uniform, $J_t(x) = J = \text{const.}$

For a system with period L , the NESS distribution reads²⁴

$$p^{\text{ss}}(x) \propto e^{-\beta U_{\text{eff}}(x)} \int_x^{x+L} dy e^{\beta U_{\text{eff}}(y)}. \quad (6)$$

The first factor is the local Boltzmann weight of the tilted potential, while the integral enforces the periodic boundary conditions and guarantees a constant probability current. Without periodicity, the distribution reduces to the tilted Boltzmann form $p^{\text{ss}}(x) \propto e^{-\beta U_{\text{eff}}(x)}$.

B. Fokker–Planck Score Learning

To embed the NESS physics into the diffusion model, we define a diffusion-time-dependent effective potential that interpolates between the physical system and the uniform prior over $\tau \in [0, 1]$

$$U_{\text{eff}}(x, \tau) = (1 - \tau) [U_\tau(x) - fx] + \tau C_{\text{prior}}, \quad (7)$$

where $U_\tau(x)$ is the potential energy at diffusion time τ , f is the constant external driving force, and C_{prior} is a normalization constant. All potentials throughout this work are expressed in units of $k_B T$. At $\tau = 0$, this reduces to the physical effective potential, while at $\tau = 1$ it yields the uniform prior distribution on the periodic domain, characterized by the constant C_{prior} .

The objective is to train a neural network $U_\tau(x)$ such that at the initial diffusion time ($\tau = 0$), $U_0^\theta(x)$ approximates the physical potential of mean force $U(x)$. Leveraging the NESS distribution, Eq. (6), and the energy-based score parameterization, the score function takes the form

$$\begin{aligned}s^\theta(x_\tau, \tau) &= \nabla \ln p^{\text{ss}}(x_\tau, \tau) \\ &= -\beta \nabla U_{\text{eff}}^\theta(x_\tau, \tau) + \Delta s^\theta(x_\tau, \tau),\end{aligned}\quad (8)$$

where $U_{\text{eff}}^\theta(x_\tau, \tau)$ is the neural network approximation of the effective potential, while only the equilibrium potential itself is parametrized by the network, i.e., $U_\tau^\theta(x, \tau) = (1 - \tau) [U_\tau^\theta(x) - fx] + \tau C_{\text{prior}}$. It should be emphasized that the correction term Δs^θ arises from the gradient of the nonlocal integral in the NESS distribution (Eq. (6)). It was found that when the neural network is constrained to output strictly periodic functions—i.e., $U_\tau^\theta(x) = U_\tau^\theta(x + L)$ —the integral over one period becomes independent of x , and therefore this term can be neglected.²⁴ This simplification motivates the use of Fourier features as network inputs (see Sec. II F) and leads to the simplified score expression used in practice

$$s^\theta(x_\tau, \tau) \approx -\beta(1 - \tau) [\nabla U_\tau^\theta(x_\tau) - f]. \quad (9)$$

C. Diffusion on Riemannian Manifolds

While the formulation above addresses periodic coordinates, estimating free energies for variables defined on non-Euclidean manifolds, such as angular coordinates, presents distinct challenges. For a polar angle θ , geometric factors introduce Jacobian singularities at the poles $\theta = 0, \pi$, which can lead to numerical instabilities in the effective potential during training. To address this, diffusion models can be formally extended to Riemannian manifolds such as $\text{SE}(3)$.^{33,34}

Here, however, we adopt a more direct approach. By employing the variable transformation $u = \cos \theta$ and the corresponding force transformation $f_u = -f_\theta / \sin \theta$, the geometric singularities are absorbed, yielding a well-defined diffusion process on the interval $u \in [-1, 1]$. The score function in the original θ coordinate is then recovered via the chain rule as

$$s^\theta(\theta_\tau, \tau) = s^\theta(u_\tau, \tau) \cdot \left| \frac{du}{d\theta} \right|. \quad (10)$$

D. Extension to Two Dimensions

The formulation above generalizes naturally to multi-dimensional collective variable spaces $\mathbf{x} = (x_1, x_2)$ with periodicities L_1 and L_2 . In the two-dimensional case, the effective potential becomes

$$U_{\text{eff}}(\mathbf{x}, \tau) = (1 - \tau) [U_\tau(\mathbf{x}) - \mathbf{f} \cdot \mathbf{x}] + C_{\text{prior}}, \quad (11)$$

where $\mathbf{f} = (f_1, f_2)$ is the vector of constant driving forces. The neural network learns a scalar potential $U_\tau^\theta(\mathbf{x})$, and the score becomes a two-dimensional vector field

$$s^\theta(\mathbf{x}_\tau, \tau) = -\beta \nabla U_{\text{eff}}^\theta(\mathbf{x}_\tau, \tau). \quad (12)$$

A key practical consideration is that not all collective variables need to be externally driven. In the lipid bilayer systems studied here, a constant force is applied along the membrane normal z (i.e., $f_z \neq 0$), while the orientational

degree of freedom θ may or may not be biased. When $\theta = 0$, the system still reaches a well-defined NESS because the θ coordinate equilibrates conditionally for each value of z . The score-based framework accommodates this naturally by simply setting the corresponding component of \mathbf{f} to zero. In contrast, for the alanine dipeptide system, constant forces are applied along both dihedral angles ϕ and ψ .

Because the neural network learns a scalar energy function, the extension to two dimensions introduces no structural changes to the architecture beyond increasing the input dimensionality. The only additional computational cost arises from the need for sufficient sampling of the two-dimensional NESS distribution.

E. Training Objective and Regularization

Training the energy-based diffusion model determines the potential energy up to a diffusion-time-dependent additive constant $C(\tau)$. The full training objective combines the denoising score matching loss with regularization terms to ensure physical consistency

$$\mathcal{L} = \mathcal{L}_{\text{DSM}} + \lambda_1 \mathcal{L}_{\text{reg}} + \lambda_2 \mathcal{L}_{\text{FP}}, \quad (13)$$

where λ_1 and λ_2 are weighting coefficients. In this work, we employ the two regularization strategies in a mutually exclusive fashion, setting either $\lambda_1 = 10^{-5}$ (with $\lambda_2 = 0$) or $\lambda_2 = 10^{-6}$ (with $\lambda_1 = 0$).

The first regularization term promotes smoothness of the learned potential with respect to the diffusion time τ^{32}

$$\mathcal{L}_{\text{reg}} = \mathbb{E}_{x_0 \sim p_0, x_\tau \sim p(x_\tau | x_0)} \left[\left\| \partial_\tau U^\theta(x_\tau, \tau) \right\|^2 \right]. \quad (14)$$

While the time-derivative regularization ensures smoothness, it does not guarantee that the learned potential adheres to the underlying physical dynamics. Furthermore, in regions of the configuration space that are not sampled, the network receives no gradient signal from the denoising objective, which can lead to unphysical extrapolations.

To address these issues, Plainer et al. suggested enforcing consistency with the Fokker–Planck equation as a physics-informed regularization, referred to as Fokker–Planck regularization.³⁵ Defining the residual of the diffusion-time-dependent Fokker–Planck equation

$$R(x, \tau) = -\nabla \cdot J_\tau(x) - \partial_\tau p_\tau(x), \quad (15)$$

where the probability current J_τ and the density p_τ are both parameterized through $U_\tau^\theta(x)$ via the NESS ansatz (Eq. (6)), the Fokker–Planck regularization reads

$$\mathcal{L}_{\text{FP}} = \mathbb{E}_{x_0 \sim \mathcal{U}, x_\tau \sim p(x_\tau | x_0)} \left[\|R(x, \tau)\|^2 \right]. \quad (16)$$

This physics-informed constraint ensures that the learned potential yields a self-consistent probability evolution,

which is particularly important in sparsely sampled regions where the denoising objective alone provides insufficient gradient information (see Sec. III).

Departing from the original formulation, we compute the expectation value over uniformly sampled initial conditions $x_0 \sim \mathcal{U}([0, 1]^d)$ and their associated noised states x_τ , rather than evaluating the residual solely on the data distribution $x_0 \sim p_0$. This strategy ensures that the physical constraints are enforced globally across the configuration space, effectively regularizing the potential even in regions left unexplored by the MD simulation.

To mitigate the computational cost of this additional objective, we employ the efficient estimator provided by Plainer et al., which enables the evaluation of the Fokker–Planck residual using only first-order spatial derivatives.³⁵

F. Enforcing Symmetries via Fourier Features

Incorporating system symmetries, particularly periodicity, directly into the neural network architecture significantly enhances the performance of Fokker–Planck Score Learning. By constraining the network to output periodic functions, the correction term Δs^θ in Eq. (8) can be neglected, simplifying the training objective.²⁴ In the one-dimensional case, this is achieved by mapping the spatial coordinate x with period L to a set of Fourier features

$$x \rightarrow \left\{ \cos \frac{2\pi n}{L} x, \sin \frac{2\pi n}{L} x \right\}_{n \in \{1, \dots, N\}}, \quad (17)$$

with the maximum mode N .

This approach can be readily generalized to two dimensions. The most general form of a smooth, periodic function on a 2D domain can be represented by a Fourier series expansion in variables ϕ, ψ with 2π -periodicity

$$f(\phi, \psi) = \sum_{n,m} \left[\alpha_{n,m} \cos n\phi \cos m\psi + \beta_{n,m} \cos n\phi \sin m\psi + \gamma_{n,m} \sin n\phi \cos m\psi + \delta_{n,m} \sin n\phi \sin m\psi \right], \quad (18)$$

with coefficients defined as

$$\alpha_{n,m} = \kappa \int_0^{2\pi} d\phi \int_0^{2\pi} d\psi f(\phi, \psi) \cos n\phi \cos m\psi, \quad (19)$$

where $\beta_{n,m}$, $\gamma_{n,m}$, and $\delta_{n,m}$ follow analogously with the respective trigonometric basis functions and the normalization constant κ defined as

$$4\pi^2 \kappa = \begin{cases} 1 & \text{if } n = m = 0, \\ 4 & \text{if } n \neq 0 \text{ and } m \neq 0, \\ 2 & \text{else.} \end{cases} \quad (20)$$

By utilizing these trigonometric basis functions as input features for the neural network, boundary conditions

are satisfied intrinsically. Specifically, for physical coordinates x and y with periodicity $L_{x/y}$, the input transformation becomes

$$(x, y) \rightarrow \begin{cases} \cos \frac{2\pi n}{L_x} x \cos \frac{2\pi m}{L_y} y, \\ \sin \frac{2\pi n}{L_x} x \cos \frac{2\pi m}{L_y} y, \\ \cos \frac{2\pi n}{L_x} x \sin \frac{2\pi m}{L_y} y, \\ \sin \frac{2\pi n}{L_x} x \sin \frac{2\pi m}{L_y} y \end{cases} . \quad (21)$$

$$n, m \in \{0, \dots, N\}$$

All trivial constant modes (including, e.g., $n = m = 0$) are omitted to avoid redundancy. Beyond periodicity, additional geometric symmetries can be imposed by selectively including or excluding specific Fourier modes. For instance, mirror symmetry with respect to $x_1 = 0$, i.e., $U(-x_1, x_2) = U(x_1, x_2)$, is enforced by retaining only cosine terms in x_1 . The specific symmetry constraints employed for each system are detailed in Sec. III.

G. Molecular Dynamics Simulations

Coarse-Grained Lipid Bilayer We employed the Martini 3 coarse-grained force field,³⁶ together with the automated workflow Martignac for lipid-bilayer simulations.³⁷ A symmetric 1-palmitoyl-2-oleoyl-sn-glycero-3-phosphocholine (POPC) bilayer was simulated with a solute modeled by the two Martini beads C1P3. All molecular dynamics simulations were carried out with GROMACS 2024.3,³⁸ adhering to the protocol of Martignac with an integration time step of $\delta t = 0.02$ ps.³⁷ Here and throughout this work, time scales for the Martini 3 coarse-grained model are expressed in picoseconds. We used a box size of $L_x = L_y = 6$ nm and $L_z = 10$ nm, with periodic boundary conditions in all three dimensions. Each run was equilibrated for 200 ps in the isothermal-isobaric (*NPT*) ensemble at $T = 298$ K and $P = 1$ bar, using a stochastic velocity-rescaling (v-rescale) thermostat³⁹ and a C-rescale barostat,⁴⁰ respectively. A semi-isotropic pressure coupling scheme was employed, with the compressibility in the z -direction set to zero to maintain a constant box height. Subsequent production runs were conducted in the canonical (*NVT*) ensemble sharing the same temperature and thermostat. We note that the use of the *NVT* ensemble was necessitated by GROMACS requirements to permit biasing across distances exceeding half the simulation box length.

We performed four independent production runs, each of 1 μ s duration, applying constant biasing forces $f \in \{4, 6, 8, 10\}$ kJ mol⁻¹ nm⁻¹. Trajectory frames were recorded every $\delta t = 0.2$ ps for subsequent analysis. For each force magnitude, an additional trajectory of 1 μ s was simulated with a moving harmonic potential applied to the θ coordinate (see Sec. III for details). This additional bias was carried out using the open-source, community-developed PLUMED library v2.⁴¹

For a comparison, we carried out umbrella sampling⁹ at a window spacing of $\delta z = 0.1$ nm covering the range $z \in [0, 4.8]$ nm, with 500 ns of simulation per window,

for a later reconstruction of the PMF using MBAR.¹³ Additionally, 50 independent equilibrium MD runs of 2 μ s each were performed to obtain a converged reference free-energy landscape, where the first 500 ns of each run are discarded for equilibration.

All-Atom Lipid Bilayer For the all-atom system, we simulated ethanol permeation through a POPC lipid bilayer. A symmetric bilayer of 100 POPC lipids solvated by 9300 TIP3P water molecules and containing a single ethanol molecule (parameterized using CGenFF⁴²) is modeled using the CHARMM36⁴³ force field and GROMACS 2025.02.³⁸ Following energy minimization and a standard six-step CHARMM-GUI⁴⁴⁻⁴⁶ equilibration protocol (1.875 ns total) utilizing the v-rescale thermostat and C-rescale barostat, two NVT production simulations were performed with an integration time step of 2 fs and $T = 308$ K. Constant-force pulling simulations were performed with $f \in \{20, 25\}$ kJ mol⁻¹ nm⁻¹, each with a duration of $t = 60$ ns. The force was applied to the ethanol center of mass along the bilayer normal, and the molecule's orientation was monitored throughout the simulation.

Alanine Di peptide We simulated the dynamics of acetyl-alanine-N-methylamide (ACE-ALA-NME) in explicit solvent. The peptide was modeled using the AMBER99SB-ILDN⁴⁷ force field and solvated in a cubic box containing 622 TIP3P water molecules and one neutralizing Na⁺/Cl⁻ ion pair. All simulations were performed using GROMACS 2025.2.³⁸

Following steepest descent energy minimization, the system was equilibrated in the NPT ensemble for 200 ps using the v-rescale thermostat ($T = 298$ K, $\tau_T = 0.1$ ps) and C-rescale barostat ($P = 1$ bar, $\tau_P = 2.0$ ps, isotropic coupling).

Production simulations were performed in the NVT ensemble at 298 K for 200 ns with an integration time step of 2 fs. To enhance sampling of the Ramachandran plane, constant-force pulling simulations were conducted by applying constant torques to the backbone torsion angles ϕ (C-N-C_α-C) and ψ (N-C_α-C-N). A set of simulations was performed with force combinations $f_{\phi, \psi} \in \{(-2, 2), (2, -2), (0, 2), (0, -2)\}$ kJ mol⁻¹ rad⁻¹. As a reference, 12 independent equilibrium MD runs of 2.4 μ s each were performed, totaling 28.8 μ s.

H. Neural Network Architecture and Training

The diffusion model was implemented using the JAX machine learning framework,⁴⁸ the Flax neural network library,⁴⁹ and the Optax optimization framework.⁵⁰

Noise Schedule An exponential noise schedule was employed,²⁵

$$\sigma_\tau = \sigma_{\min}^{1-\tau} \sigma_{\max}^\tau , \quad (22)$$

where σ_{\min} and σ_{\max} denote the minimum and maximum noise levels, respectively. For all systems, σ_{\max} was set to $L/2$, ensuring that the noising process reaches the uniform latent distribution. The minimum noise level was set to $\sigma_{\min} = 0.005$ for the lipid systems to ensure high spatial resolution in the learned potential energy function, while for alanine dipeptide we used a larger minimal noise $\sigma_{\min} = 0.01$ to restrict overfitting.

Optimization To ensure consistency, all models were trained for 50 epochs using the AdamW optimizer⁵¹ with a mini-batch size of 512. The learning rate followed an initial linear warm-up from 5×10^{-7} to 5×10^{-3} over the first 5 epochs, followed by a cosine decay to 5×10^{-7} for the remaining epochs. All available trajectory frames were used for training, corresponding to a sampling interval of $\Delta t = 0.02$ ps for alanine dipeptide, and $\Delta t = 0.2$ ps and $\Delta t = 0.06$ ps for the coarse-grained and all-atom lipid bilayer systems, respectively.

Architecture The neural network consisted of a fully connected architecture with the Swish activation function⁵² to ensure differentiability. For the lipid systems (coarse-grained and all-atom), the network comprised five hidden layers of 64 neurons each, while for alanine dipeptide, 3 layers of 48 neurons each were used.

III. RESULTS AND DISCUSSION

A. Alanine Dipeptide

We begin with alanine dipeptide solvated in water, a system characterized by two intrinsically periodic collective variables: the backbone dihedral angles ϕ and ψ . This application represents a direct extension of the one-dimensional FPPL framework²⁴ to two dimensions, as both coordinates are periodic and can be driven by constant biasing torques. In contrast to the lipid bilayer system, where the periodicity of the system results from the periodic boundary conditions of the simulation box, here the periodicity arises from the molecular structure itself—specifically the dihedral angles.

As a reference, we performed 12 independent equilibrium MD simulations of 2.4 μ s each, totaling 28.8 μ s. The resulting free-energy landscape as a function of the dihedral angles ϕ and ψ is shown in Fig. 2a. For the non-equilibrium MD simulations, we applied constant biasing forces $f_{\phi,\psi} = (0, \pm 2) \text{ kJ mol}^{-1} \text{ rad}^{-1}$ and $f_{\phi,\psi} = (\mp 2, \pm 2) \text{ kJ mol}^{-1} \text{ rad}^{-1}$, simulating 200 ns for each force combination.

Although both dihedral angles are periodic, the constant biasing torques are less effective at enhancing sampling than in the membrane systems discussed below. The steric clash near $\phi \approx 2\pi$ effectively confines ϕ , making it behave akin to a non-periodic coordinate. While

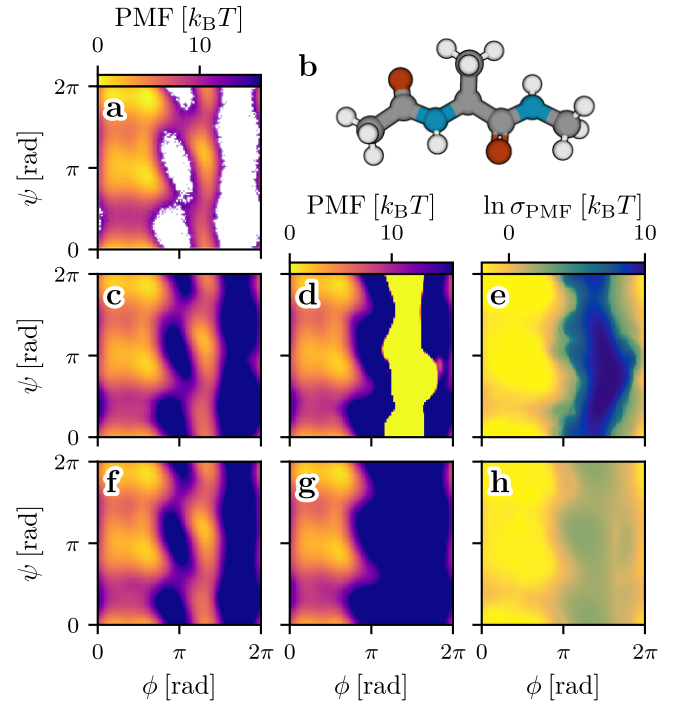


FIG. 2. Free-energy estimation of alanine dipeptide in water: (a) Reference Ramachandran plot of the free-energy landscape as a function of the dihedral angles ϕ and ψ . (b) Depiction of alanine dipeptide. (c–h) Reconstructed free-energy landscapes from 23 ns of non-equilibrium MD data, with (c, f) and without (d, g) sampling of the α_L region. The upper row corresponds to the simple energy regularization and the lower row to the Fokker–Planck regularization. (e+h) The standard deviation across 50 independent runs for the simple energy regularization and the Fokker–Planck regularization, respectively.

this limitation could be mitigated by introducing a time-dependent biasing potential, we purposefully retain this setup to demonstrate the impact of insufficient sampling of relevant degrees of freedom on the reconstruction of the free-energy landscape.

Figure 2c+d depicts the reconstructed free-energy landscapes derived from 11.5 ns of MD simulation data for each force combination, $f_{\phi,\psi} = (\mp 2, \pm 2) \text{ kJ mol}^{-1} \text{ rad}^{-1}$, amounting to a cumulative sampling time of 23 ns. In Fig. 2c we select an individual run where the left-handed α -helix region (α_L) was sampled, whereas in Fig. 2d we show a run where this region remained unexplored. While both reconstructions successfully recover the main free-energy basins ($\phi < \pi$), the lack of sampling in the α_L region in Fig. 2d results in an arbitrary network output. This behavior arises because the neural network is never exposed to samples in this region during training, and consequently, the objective function provides no gradient to guide the potential energy surface prediction in this area.

To address this issue, we employ the Fokker–Planck

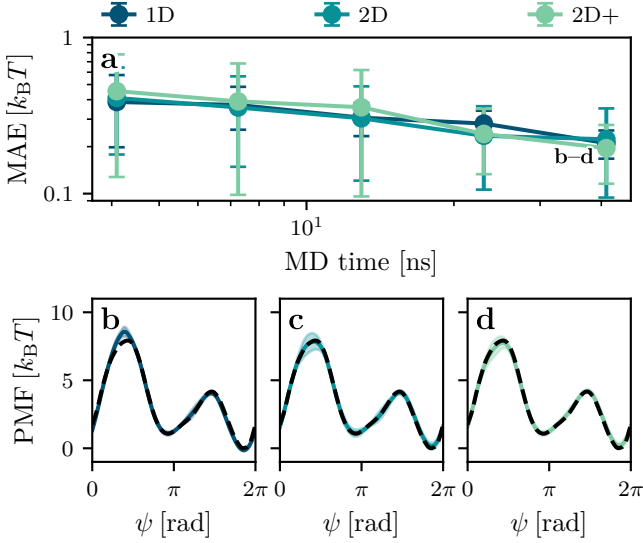


FIG. 3. Performance evaluation of Fokker-Planck Score Learning (FPSL) for reconstructing the one-dimensional free-energy profile of alanine dipeptide along the ψ dihedral angle. (a) Mean absolute error (MAE) as a function of the aggregate MD simulation time. The comparison includes: FPSL trained solely on ψ (1D); FPSL trained on the joint space (ϕ, ψ) with biasing applied only along ϕ (2D); and FPSL trained on (ϕ, ψ) with biasing applied along both ϕ and ψ (2D+). For the 2D approaches, the Fokker-Planck regularization scheme is employed, and the corresponding 1D profile is derived by marginalizing over ϕ . (b-d) Comparison of the free-energy profiles reconstructed by FPSL using approximately 41 ns of non-equilibrium MD data for the 1D (b), 2D (c), and 2D+ (d) methodologies.

regularization,³⁵ as outlined in section II. This approach imposes a physics-informed constraint on the learned energy landscape, ensuring consistency with the stationarity condition of the Fokker-Planck equation. Incorporating this regularization leads to a significant improvement in the reconstruction of the unsampled α_L region, as shown in Fig. 2f+g. With this constraint, FPSL robustly identifies the unsampled area as a high-energy state. Notably, when α_L is adequately sampled, both regularization schemes yield virtually identical free-energy landscapes.

To quantify these observations, Fig. 2e+h displays the logarithm of the standard deviation across 50 independent training runs for both regularization methods. It is evident that while both approaches converge clearly within the sampled regions, the Fokker-Planck regularization exhibits a significantly reduced standard deviation in the unsampled α_L region. In contrast, the simple energy regularization is prone to numerical artifacts and high variance in the absence of data.

Finally, we evaluate the performance of FPSL in reconstructing the one-dimensional free-energy profile along the ψ dihedral angle. Because the orthogonal coordinate ϕ exhibits slow relaxation dynamics compared to ψ , the Fokker-Planck regularization scheme is employed

throughout the following analysis to ensure robust learning of the energy landscape.

Figure 3a presents the convergence of the MAE as a function of the accumulated MD simulation time. Three distinct approaches are compared: (i) direct learning of the 1D free-energy profile along ψ (1D); (ii) learning the 2D free-energy landscape in (ϕ, ψ) followed by marginalization over ϕ (2D); and (iii) learning the 2D landscape while additionally biasing the ϕ coordinate (2D+). Although all three methods converge to a comparable error of approximately $0.2 k_B T$ after an aggregate simulation time of 41 ns, the 2D/2D+ approaches demonstrate slightly faster convergence behavior. However, it is observed that the standard deviation across 50 independent training runs is notably higher for the 2D and 2D+ approaches compared to the 1D case. This increased variance can likely be attributed to the sparse sampling of the slow ϕ degree of freedom.

The reconstructed free-energy profiles obtained from approximately 41 ns of MD simulation data are visualized in Fig. 3b-d for the 1D, 2D, and 2D+ approaches, respectively. While all three methods successfully capture the principal features of the reference profile, the 1D approach exhibits a systematic bias in the barrier region near $\psi \approx \pi/2$. This deviation is identified as a consequence of insufficient sampling in the α_L region (cf. Fig. 2a). Learning the full 2D landscape and subsequently marginalizing over ϕ (2D) effectively mitigates this bias. It is worth noting that the left-handed α -helix (α_L) constitutes only a small fraction of the total equilibrium probability mass. Consequently, neglecting this region in our reference equilibrium simulations introduces only a minor deviation in the 1D free-energy profile along ψ , resulting in a baseline error of approximately $0.18 k_B T$, which is comparable to the accuracy achieved by our FPSL results.

B. Coarse-Grained Lipid Bilayer

We next turn to the lipid bilayer, a fundamental structural component of biological membranes whose free-energy landscape governs critical phenomena such as solute permeation. In contrast to the alanine dipeptide system, where both collective variables are periodic dihedral angles, the lipid bilayer introduces a qualitatively different challenge: one of the two relevant collective variables—the polar angle θ characterizing the solute orientation—is intrinsically non-periodic. This extends the FPSL framework beyond purely periodic CV spaces and demonstrates its flexibility in handling mixed coordinate types. In previous work, we introduced Fokker-Planck Score Learning (FPSL) as a method to reconstruct free-energy landscapes from non-equilibrium steady-state simulations.²⁴ Therein, the efficiency of the method relative to conventional umbrella sampling combined with the multistate Bennett acceptance ratio (MBAR) estimator was established by re-

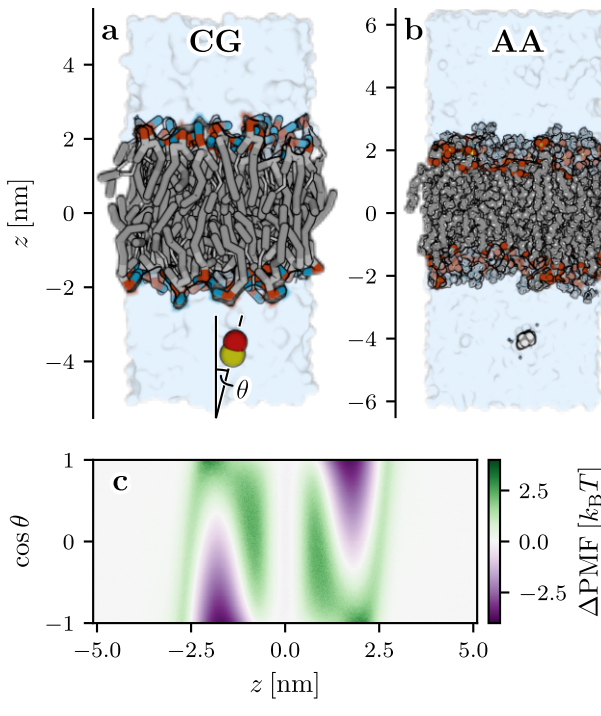


FIG. 4. Molecular systems studied: (a) Coarse-grained Martini 3 model of a C1P3 molecule permeating a POPC lipid bilayer. (b) All-atom model of an ethanol molecule permeating a POPC lipid bilayer. (c) Free-energy landscape of C1P3 permeating a POPC lipid bilayer, shown in panel (a), as a function of the normal distance z from the bilayer midplane and $\cos \theta$, where θ is the polar angle of the molecule.

constructing the one-dimensional free-energy profile of a single Martini bead permeating a 1-palmitoyl-2-oleoyl-sn-glycero-3-phosphocholine (POPC) bilayer.

In the present study, we extend FPSL to systems of increased complexity to demonstrate: (i) its robustness in reconstructing one-dimensional free-energy profiles even when relevant orthogonal degrees of freedom are marginalized, and (ii) its capacity to reconstruct full two-dimensional free-energy landscapes with negligible computational overhead compared to the one-dimensional case. Specifically, we employ the coarse-grained Martini force field to investigate the permeation of a solute composed of C1 and P3 beads through a POPC bilayer, as illustrated in Fig. 4a. A detailed description of the molecular dynamics simulation parameters is provided in Sec. II G.

The system dynamics are primarily characterized by two collective variables: (i) the normal distance of the center of mass of C1P3 from the bilayer midplane, denoted by z , and (ii) the polar angle θ between the bilayer normal and the vector connecting the C1 and P3 beads (see Fig. 4a). The regions $z < 0$ and $z > 0$ correspond to the lower and upper leaflets, respectively. Given the amphiphilic nature of the solute (hydrophobic C1, hydrophilic P3), the polar angle θ plays a significant role in

determining the insertion free energy. The resulting two-dimensional free-energy landscape as a function of z and $\cos \theta$ is depicted in Fig. 4c. It features two symmetric minima at $(z, \cos \theta) \approx (\pm 1.8 \text{ nm}, \pm 1)$, corresponding to the preferred orientation of the molecule in each leaflet, with the hydrophobic C1 bead oriented toward the bilayer core.

We begin by reconstructing the 1D free-energy profile along the z -coordinate, a metric commonly used to characterize solute permeation through lipid bilayers. Here, we compare the performance of FPSL when learning the 1D FEL directly versus learning the 2D FEL along z and θ and subsequently marginalizing over θ . To sample the non-equilibrium steady state, we employ biased MD simulations by applying constant forces to the C1P3 molecule along the z -direction of $f \in \{4, 6, 8, 10\} \text{ kJ mol}^{-1} \text{ nm}^{-1}$, each for a duration of $t = 1 \mu\text{s}$. For each force magnitude, an additional trajectory of $1 \mu\text{s}$ is simulated with a moving harmonic potential applied to the θ coordinate, a technique commonly utilized in steered MD biasing

$$f_\theta(t) = \kappa \left[\frac{\pi}{2} \left(1 + \sin \frac{2\pi t}{\tau} \right) - \theta \right] \quad (23)$$

with $\kappa = 0.5 \text{ kJ mol}^{-1} \text{ rad}^{-2}$ and $\tau = 39.813 \text{ ps}$. It is important to note that, as θ is not periodic, a constant force would bias the system towards $\theta = \pi$ rather than enhancing sampling. Furthermore, the period is chosen such that it is not a multiple of the integration step, ensuring adequate coverage.

As a reference, we utilize equilibrium simulations with a total duration of $97.5 \mu\text{s}$, obtained from 50 independent MD runs. From these, the free-energy profile along z is derived via Fourier expansion of the binned data. This profile, shown in Fig. 5c-d as a black dashed line, serves as a benchmark for evaluating the performance of our FPSL method. We quantify accuracy via the mean absolute error (MAE) of the reconstructed free-energy profiles $U(z)$ relative to this reference

$$\text{MAE} = \langle |U(z) - U_{\text{ref}}(z)| \rangle_z. \quad (24)$$

Following the methodology established in our previous work,²⁴ we utilize Fourier features to parametrize the neural network representing the potential energy function $U^\theta(x)$. For the 1D free-energy profile along z , we exploit the system's symmetry with respect to the bilayer midplane, i.e., $U(-z) = U(z)$. This symmetry is enforced by restricting the network parametrization to cosine Fourier modes, utilizing the first $N = 8$ modes. For the 2D free-energy landscape along z and θ , we leverage two geometric properties: (i) the central symmetry of the landscape around $(0, \pi/2)$, implying $U(-z, \theta) = U(z, \pi - \theta)$, and (ii) the reflective boundary conditions of the θ coordinate at $\theta = 0$ and $\theta = \pi$. The latter is enforced by mapping θ to a 2π -periodic coordinate described solely by even (cosine) modes. We parametrize the neural network by retaining

all Fourier modes (see section II F) that satisfy the requested symmetries. Introducing the shifted coordinate $\vartheta = \theta - \pi/2$, this yields

$$\left\{ \cos \frac{2\pi n}{L} z \cos 2m\vartheta, \sin \frac{2\pi n}{L} z \sin (2m+1)\vartheta \right\}_{n,m} \quad (25)$$

where the number of modes is limited to $N = 4$, and the factor of 2 in the ϑ modes ensures evenness in θ . The trivial mode $n = m = 0$ is excluded.

To facilitate the training of the 2D free-energy landscape, the potential is learned as a function of $U(z, \cos \theta)$ rather than $U(z, \theta)$. This transformation results in a uniform FEL in the water phase, thereby improving training efficiency. Correspondingly, the forces in θ are scaled by $f_{\cos \theta} = -f_\theta / \sin \theta$ to account for the change of variables.

To evaluate method performance, the neural network was trained using datasets of varying trajectory lengths, $t \in [12.8, 256]$ ns for each force. These datasets comprised segments randomly selected from each constant-force simulation. To assess the uncertainty of the reconstructed profiles, this procedure was repeated for 50 independent random selections and subsequent network trainings for each trajectory length. For comparison with conventional umbrella sampling–based MBAR, simulations were conducted with a window spacing of $\delta z = 0.1$ nm over the range $z \in [0, 4.8]$ nm. Each window was simulated for $t = 500$ ns, resulting in a total simulation time of 24.5 μ s. To estimate uncertainty, MBAR was applied to trajectory segments of lengths $t \in [1, 68]$ ns from each window.

Figure 5a displays the MAE of MBAR versus FPSL using only z as input (1D), z and θ as input (2D), and additionally biasing θ (2D+) as a function of the accumulated MD simulation time. All three FPSL variants are observed to converge significantly faster than MBAR. Consequently, we compare in Fig. 5b the relative change in MAE between the 1D and 2D approaches, defined as

$$\Delta \text{MAE} = \langle \text{MAE}_{1\text{D}} - \text{MAE}_{2\text{D}} \rangle. \quad (26)$$

It is found that learning the full 2D landscape and subsequently marginalizing over $\cos \theta$ (2D) yields a comparable MAE to learning the 1D landscape directly (1D). Thus, reconstructing the full 2D FEL does not introduce additional uncertainty into the marginalized 1D free-energy profile. However, when θ is additionally biased (2D+), a slight improvement in the MAE is observed. The magnitude of this improvement is small, presumably because the sampling along θ is already sufficient when biasing only along z , due to the significantly faster relaxation time of θ compared to z . For the same reason, neglecting θ in the 1D case (or in MBAR) does not substantially impact performance.

It should be noted that when dealing with coordinates lacking a uniform measure, such as polar angles, it can be advantageous to learn the FEL using $\cos \theta$ rather than θ directly, as this results in a uniform measure in the latent space (see Fig. 4c). Indeed, we find that employing $\cos \theta$ leads to a minor improvement, as shown in Fig. 5b.

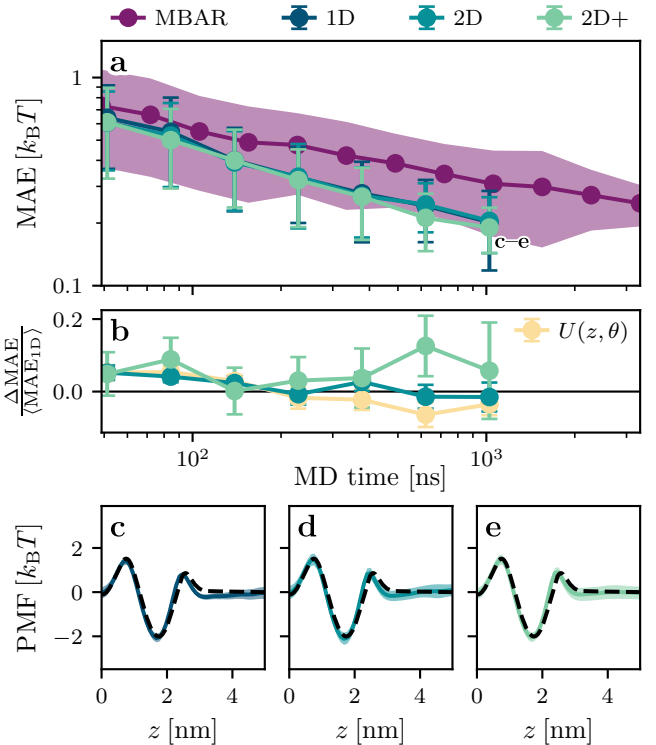


FIG. 5. Performance evaluation of Fokker-Planck Score Learning (FPSL) for reconstructing the free-energy profile of C1P3 permeation through a POPC lipid bilayer. (a) Mean absolute error (MAE) as a function of aggregate MD simulation time. Comparison includes: FPSL trained on z (1D); FPSL trained on $(z, \cos \theta)$ with biasing along z (2D); FPSL trained on $(z, \cos \theta)$ with biasing along both z and θ (2D+); and umbrella sampling with MBAR (purple). For the 2D methods, the 1D profile is obtained by marginalizing over $\cos \theta$. (b) Convergence improvement (ΔMAE) achieved by learning the full 2D landscape (and subsequently marginalizing) compared to learning the 1D landscape directly. The yellow curve represents the 2D reconstruction using θ instead of $\cos \theta$. (c–e) Comparison of free-energy profiles reconstructed by FPSL using approximately 1 μ s of MD simulation data.

To visualize these findings, Fig. 5c–e present the mean and variance of the reconstructed free-energy profiles using approximately 1 μ s of MD simulation data for the 1D, 2D, and 2D+ approaches, respectively. All three FPSL approaches yield profiles in good agreement with the reference (black dashed line), with the 2D+ approach exhibiting the closest correspondence. While the 1D approach displays the smallest variance, it exhibits a slight bias in the barrier region at $z \approx 2.5$ nm, which is mitigated when learning the full 2D landscape. This bias likely arises because, under strong pulling forces, the molecule lacks sufficient time to reorient from $\theta \approx 0$ to $\theta \approx \pi$ as it exits the membrane. Consequently, the system attempts an insertion in an unfavorable orientation, introducing a systematic bias in the calculated free-energy profile.

Subsequently, we assess the performance of FPSL in re-

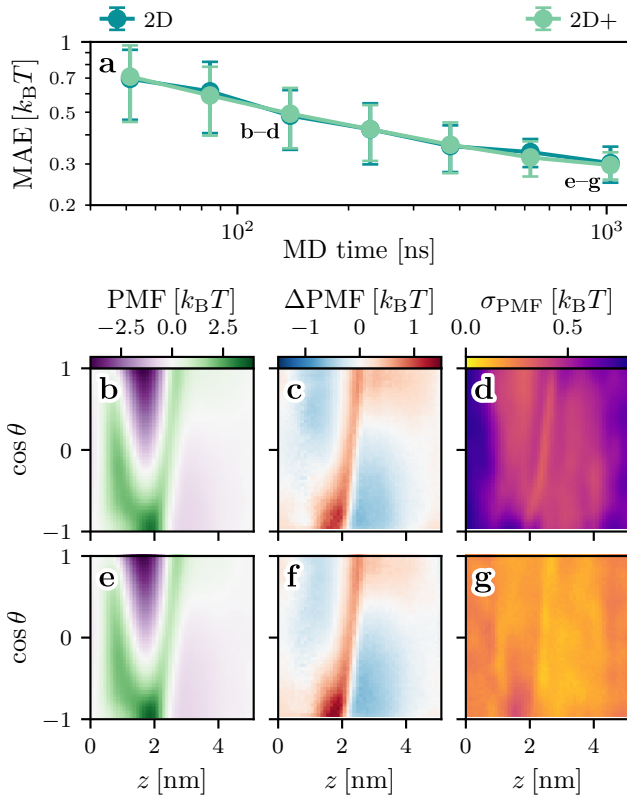


FIG. 6. Performance of Fokker-Planck Score Learning (FPSL) in reconstructing the 2D free-energy landscape of C1P3 permeating a POPC lipid bilayer. (a) Convergence of the 2D mean absolute error (MAE) as a function of aggregate MD simulation time, comparing FPSL trained on $(z, \cos \theta)$ with biasing applied only along z (2D) versus biasing applied along both z and θ (2D+). (b–g) Analysis of the landscapes learned by the 2D method (bias on z only) using approximately 139 ns (top row) and 1 μ s (bottom row) of data. Panels show the (b, e) average reconstructed FEL, (c, f) difference to the reference FEL, and (d, g) the standard deviation across 50 independent training runs.

constructing the full 2D free-energy landscape as a function of z and $\cos \theta$. We compare the performance of FPSL when biasing solely along z (2D) versus biasing along both z and θ (2D+), as shown in Fig. 6a. Notably, these results utilize the same training data as the 1D analysis above, but without marginalization over $\cos \theta$. Both methods are found to converge to virtually identical MAE values, reaching approximately $0.32 k_B T$ after 1 μ s of aggregate MD simulation time, compared to approximately $0.24 k_B T$ in the 1D case.

In Fig. 6b–g, we analyze the reconstructed 2D free-energy landscape utilizing the 2D method (biasing only along z) after approximately 139 ns (top row) and 1 μ s (bottom row) of MD simulation data, averaged over 50 independent training runs. In both instances, the principal features of the free-energy landscape are accurately reconstructed, including the minimum at $(z, \cos \theta) \approx (1.8 \text{ nm}, 1)$, the U-shaped barrier region surrounding it,

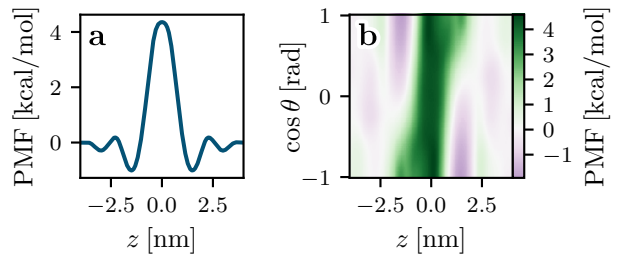


FIG. 7. Free-energy landscape of ethanol permeating a POPC lipid bilayer modeled at the all-atom level (see Fig. 4b), reconstructed using Fokker-Planck Score Learning (FPSL). The landscape is depicted as a function of the normal distance z from the bilayer midplane and the cosine of the polar angle, $\cos \theta$. (a) Marginalized 1D free-energy profile obtained by integrating over $\cos \theta$, and (b) the full reconstructed 2D landscape.

and the uniform free energy in the water phase (see 6b+e). However, upon comparison with the reference FEL, FPSL exhibits a small systematic bias, specifically an overestimation of the barrier height (indicated in dark red), see 6c+f. This deviation is presumably attributable to the sparse sampling of this high-energy region in the non-equilibrium steady-state data, which results in higher uncertainty in the reconstructed landscape. Examination of the standard deviation across the 50 independent training runs (see 6d+g) reveals uniform convergence across the landscape as sampling increases.

C. All-Atom Lipid Bilayer

Having established and benchmarked the performance of FPSL on a coarse-grained model with a non-periodic orientational degree of freedom, we now demonstrate its applicability at all-atom resolution: the permeation of ethanol through a POPC lipid bilayer (see Fig. 4). This system has been previously investigated by Comer et al., who reported a 2D free-energy landscape.⁵³ Consistent with their work, we characterize the system using two collective variables: (i) the normal distance z of the ethanol center of mass from the bilayer midplane, and (ii) the polar angle θ between the z -axis and the vector $r_{\text{Et}} - r_{\text{OH}}$, where r_{OH} and r_{Et} denote the centers of mass of the hydroxyl and ethyl groups, respectively.

We perform constant-force pulling simulations with $f \in \{20, 25\} \text{ kJ mol}^{-1} \text{ nm}^{-1}$, each with a duration of $t = 60 \text{ ns}$, resulting in 10 and 14 membrane permeation events, respectively. Analogous to the coarse-grained case, we enforce point symmetry around $(z, \theta) = (0, \pi/2)$ as well as reflective boundary conditions at $\theta = 0$ and $\theta = \pi$ by employing the Fourier features defined in Eq. (25) with $N = 4$. Using FPSL, we reconstruct the 2D free-energy landscape as a function of z and $\cos \theta$, shown in Fig. 7b.

As described by Comer et al., the free-energy landscape exhibits distinct features: (i) two minima at $(z, \cos \theta) \approx$

(± 1.5 nm, ± 1), corresponding to an orientation where the hydroxyl group points toward the water phase while the ethyl group is buried in the hydrophobic core; and (ii) an S-shaped barrier region spanning approximately 2 nm. Regarding the barrier height, we obtain a value of approximately 4 kcal mol⁻¹, which is in reasonable agreement with the value of ≈ 3.0 kcal mol⁻¹ reported by Comer et al. For the depth of the minima, we observe slightly larger values (1.8 kcal mol⁻¹) compared to the reference (1.0 kcal mol⁻¹). This discrepancy can be attributed to the different coordinate representations: Comer et al. computed $U(z, \theta)$, which implicitly includes the Jacobian term $-k_B T \ln \sin \theta$, resulting in shallower minima near the poles ($\theta = 0, \pi$). It should be noted that while our result, $U(z, \cos \theta)$, yields a uniform free energy in the bulk water phase, which corresponds to the expected physical behavior, the uniformity observed in the reference work in the bulk water phase suggests potential sampling or convergence limitations in the original study.

The 1D free-energy profile for ethanol permeation has also been reported by Ghorbani et al.⁵⁴. They observed that the permeation barrier increases with decreasing ethanol concentration, rising from 3.3 ± 1.0 $k_B T$ to 6.3 ± 0.1 $k_B T$ as the concentration drops from 18 mol % to 1 mol %. Our simulation of a single ethanol molecule corresponds to the dilute limit (< 0.01 mol %). We find a barrier of approximately 4.2 kcal mol⁻¹ (approx. 6.9 $k_B T$), which is in excellent agreement with their results at low concentration.

Comer et al. employed adaptive biasing force (ABF) simulations to reconstruct the 2D free-energy landscape. Although the computational cost for the 2D surface was not explicitly reported, a subsequent study noted that generating 1D free-energy profiles for ethanol permeation across various bilayers required approximately 2–4 μ s of sampling.⁵⁵ In contrast, Ghorbani et al. reported that approximately 0.5 μ s was sufficient to reconstruct the 1D free-energy profile of ethanol in POPC using maximum likelihood estimation.^{54,56} Our FPSL approach enables the reconstruction of the full 2D free-energy landscape with as little as 120 ns of MD simulation, representing a significant reduction in computational cost compared to these established methods. Specifically, this corresponds to more than an order-of-magnitude speedup relative to ABF-based approaches and approximately a fourfold reduction compared to maximum likelihood estimation, while simultaneously providing the full two-dimensional landscape rather than only a one-dimensional projection.

IV. CONCLUSION

In this work, we have extended the Fokker–Planck Score Learning (FPSL) framework to reconstruct multidimensional free-energy landscapes from non-equilibrium molecular dynamics simulations. By incorporating orthogonal degrees of freedom into the learning process, we demonstrated that FPSL can recover full two-

dimensional landscapes with negligible computational overhead compared to one-dimensional profiles. We validated this approach on systems of varying complexity, from the conformational dynamics of alanine dipeptide—where both collective variables are periodic dihedral angles—to coarse-grained and all-atom lipid bilayer permeation, where the orientational degree of freedom θ is intrinsically non-periodic. Remarkably, for the all-atom lipid bilayer, FPSL reconstructs the full 2D free-energy landscape from only 120 ns of MD simulation—around an order of magnitude less than ABF-based approaches and maximum likelihood estimation, both of which yield only one-dimensional profiles.

Importantly, because FPSL learns a smooth score function rather than relying on histogram-based densities like most established methods, incorporating a second collective variable incurs minimal additional cost during the learning phase. Our results show that while direct one-dimensional learning is often already accurate, explicitly learning the joint free-energy landscape can prevent small systematic biases that can arise when orthogonal degrees of freedom relax slowly or are strongly perturbed by external forces. Specifically, in the case of alanine dipeptide, resolving the ϕ degree of freedom corrected deviations in the barrier region. Furthermore, we showed that appropriate coordinate transformations, such as learning in $\cos \theta$ space, can significantly enhance training efficiency by ensuring a more uniform probability measure. Notably, the framework handles also non-periodic collective variables naturally, requiring only that their boundary conditions allow for mapping to a periodic domain. Furthermore, we demonstrated the efficacy of the Fokker–Planck regularization in systems with complex energy landscapes, such as alanine dipeptide. While standard score matching can yield arbitrary potentials in unsampled regions, enforcing consistency with the stationary solution of the Fokker–Planck equation ensures that high-energy states are robustly identified even in the absence of direct sampling. This physics-informed constraint effectively guides the neural network in data-sparse regimes, dramatically reducing the variance of the reconstructed landscape and ensuring physically meaningful predictions. Making FPSL numerically robust to sparsely sampled regions is a crucial step towards estimating higher-dimensional free-energy landscapes, $D > 2$.

The ability to efficiently reconstruct multidimensional free-energy surfaces opens new avenues for studying complex biomolecular processes. Future work will focus on scaling FPSL to even higher-dimensional reaction coordinates and integrating it with advanced sampling strategies to explore rare events. We anticipate that the combination of data-efficient score-based learning with robust physics-informed regularization will become a powerful tool for characterizing the thermodynamics and kinetics of molecular systems.

ACKNOWLEDGMENTS

We dedicate this work to Kurt Kremer on the occasion of his 70th birthday—an inspiring and cherished mentor to T.B. The community owes a great debt to Kremer’s seminal work in soft-matter physics and multiscale simulations, systematically aiming for simple, clear, and elegant modeling choices to further our understanding of complex liquids.

We are grateful to Jeffrey Comer for helpful discussions and Luis J. Walter and Sander Hummerich for their valuable feedback on the manuscript.

We acknowledge support by the Deutsche Forschungsgemeinschaft (DFG, German Research Foundation) under Germany’s Excellence Strategy EXC 2181/1 - 390900948 (the Heidelberg STRUCTURES Excellence Cluster) and Heidelberg University through the Research Council of the Field of Focus 2 “Patterns and Structures in Mathematics, Data, and the Material World.”

DATA AVAILABILITY STATEMENT

A Python package implementing the Fokker–Planck Score Learning framework is available under an open-source license at <https://github.com/BereauLab/fokker-planck-score-learning>.

- ¹C. Chipot and A. Pohorille, *Free energy calculations*, Vol. 86 (Springer, 2007).
- ²N. Hansen and W. F. Van Gunsteren, “Practical aspects of free-energy calculations: a review,” *J. Chem. Theory Comput.* **10**, 2632–2647 (2014).
- ³D. Frenkel and B. Smit, *Understanding molecular simulation: from algorithms to applications* (Elsevier, 2023).
- ⁴R. B. Best and G. Hummer, “Reaction coordinates and rates from transition paths,” *Proc. Natl. Acad. Sci.* **102**, 6732–6737 (2005).
- ⁵A. Laio and M. Parrinello, “Escaping free-energy minima,” *Proc. Natl. Acad. Sci.* **99**, 12562–12566 (2002).
- ⁶E. Darve, D. Rodríguez-Gómez, and A. Pohorille, “Adaptive biasing force method for scalar and vector free energy calculations,” *J. Chem. Phys.* **128**, 144120 (2008).
- ⁷Y. Sugita and Y. Okamoto, “Replica-exchange molecular dynamics method for protein folding,” *Chem. Phys. Lett.* **314**, 141–151 (1999).
- ⁸D. Hamelberg, J. Mongan, and J. A. McCammon, “Accelerated molecular dynamics: a promising and efficient simulation method for biomolecules,” *J. Chem. Phys.* **120**, 11919–11929 (2004).
- ⁹G. M. Torrie and J. P. Valleau, “Nonphysical sampling distributions in monte carlo free-energy estimation: Umbrella sampling,” *J. Comput. Phys.* **23**, 187–199 (1977).
- ¹⁰B. Roux, “The calculation of the potential of mean force using computer simulations,” *Comput. Phys. Commun.* **91**, 275–282 (1995).
- ¹¹S. Kumar, J. M. Rosenberg, D. Bouzida, R. H. Swendsen, and P. A. Kollman, “The weighted histogram analysis method for free-energy calculations on biomolecules. i. the method,” *J. Comput. Chem.* **13**, 1011–1021 (1992).
- ¹²J. S. Hub, B. L. de Groot, and D. van der Spoel, “g_wham—a free weighted histogram analysis implementation including robust error and autocorrelation estimates,” *J. Chem. Theory Comput.* **6**, 3713–3720 (2010).
- ¹³M. R. Shirts and J. D. Chodera, “Statistically optimal analysis of samples from multiple equilibrium states,” *J. Chem. Phys.* **129**, 124105 (2008).
- ¹⁴M. Orsi and J. W. Essex, “Passive permeation across lipid bilayers: a literature review,” *Mol. Simul. Biomembr. Biophys. To Funct.* **76** (2010).
- ¹⁵I. Buch, S. K. Sadiq, and G. De Fabritiis, “Optimized potential of mean force calculations for standard binding free energies,” *J. Chem. Theory Comput.* **7**, 1765–1772 (2011).
- ¹⁶R. V. Swift and R. E. Amaro, “Back to the future: can physical models of passive membrane permeability help reduce drug candidate attrition and move us beyond qspr?” *Chem. Biol. & Drug Des.* **81**, 61–71 (2013).
- ¹⁷T. S. Carpenter, D. A. Kirshner, E. Y. Lau, S. E. Wong, J. P. Nilmeier, and F. C. Lightstone, “A method to predict blood-brain barrier permeability of drug-like compounds using molecular dynamics simulations,” *Biophys. J.* **107**, 630–641 (2014).
- ¹⁸C. T. Lee, J. Comer, C. Herndon, N. Leung, A. Pavlova, R. V. Swift, C. Tung, C. N. Rowley, R. E. Amaro, C. Chipot, *et al.*, “Simulation-based approaches for determining membrane permeability of small compounds,” *J. Chem. Inf. Model.* **56**, 721–733 (2016).
- ¹⁹B. J. Bennion, N. A. Be, M. W. McNerney, V. Lao, E. M. Carlson, C. A. Valdez, M. A. Malfatti, H. A. Enright, T. H. Nguyen, F. C. Lightstone, *et al.*, “Predicting a drug’s membrane permeability: A computational model validated with in vitro permeability assay data,” *J. Phys. Chem. B* **121**, 5228–5237 (2017).
- ²⁰C. H. Tse, J. Comer, Y. Wang, and C. Chipot, “Link between membrane composition and permeability to drugs,” *J. Chem. Theory Comput.* **14**, 2895–2909 (2018).
- ²¹R. Menichetti, K. H. Kanekal, K. Kremer, and T. Bereau, “In silico screening of drug-membrane thermodynamics reveals linear relations between bulk partitioning and the potential of mean force,” *J. Chem. Phys.* **147**, 125101 (2017).
- ²²R. Menichetti, K. H. Kanekal, and T. Bereau, “Drug–membrane permeability across chemical space,” *ACS Cent. Sci.* **5**, 290–298 (2019).
- ²³C. Jarzynski, “Nonequilibrium equality for free energy differences,” *Phys. Rev. Lett.* **78**, 2690 (1997).
- ²⁴D. Nagel and T. Bereau, “Fokker–planck score learning: Efficient free-energy estimation under periodic boundary conditions,” *J. Phys. Chem. B* **129**, 11780–11790 (2025).
- ²⁵Y. Song, J. Sohl-Dickstein, D. P. Kingma, A. Kumar, S. Ermon, and B. Poole, “Score-based generative modeling through stochastic differential equations,” *arXiv cs.LG* (2020), 10.48550/arXiv.2011.13456.
- ²⁶H. Risken, *Fokker–planck equation* (Springer, 1996).
- ²⁷J. Sohl-Dickstein, E. A. Weiss, N. Maheswaranathan, and S. Ganguli, “Deep unsupervised learning using nonequilibrium thermodynamics,” *arXiv cs.LG* (2015), 10.48550/arXiv.1503.03585.
- ²⁸J. Ho, A. Jain, and P. Abbeel, “Denoising diffusion probabilistic models,” *arXiv cs.LG* (2020), 10.48550/arXiv.2006.11239.
- ²⁹B. D. Anderson, “Reverse-time diffusion equation models,” *Stoch. Process. Their Appl.* **12**, 313–326 (1982).
- ³⁰M. Arts, V. Garcia Satorras, C.-W. Huang, D. Zugner, M. Fedreric, C. Clementi, F. Noé, R. Pinsky, and R. van den Berg, “Two for one: Diffusion models and force fields for coarse-grained molecular dynamics,” *J. Chem. Theory Comput.* **19**, 6151–6159 (2023).
- ³¹B. Máté, F. Fleuret, and T. Bereau, “Neural thermodynamic integration: Free energies from energy-based diffusion models,” *J. Phys. Chem. Lett.* **15**, 11395–11404 (2024).
- ³²B. Máté, F. Fleuret, and T. Bereau, “Solvation free energies from neural thermodynamic integration,” *J. Chem. Phys.* **162**, 11395–11404 (2025).
- ³³G. Corso, H. Stärk, B. Jing, R. Barzilay, and T. Jaakkola, “Diffdock: Diffusion steps, twists, and turns for molecular docking,” *arXiv q-bio.BM* (2022), 10.48550/arxiv.2210.01776.
- ³⁴J. Yim, B. L. Trippe, V. De Bortoli, E. Mathieu, A. Doucet, R. Barzilay, and T. Jaakkola, “Se(3) diffusion model with ap-

- plication to protein backbone generation," arXiv cs.LG (2023), 10.48550/arxiv.2302.02277.
- ³⁵M. Plainer, H. Wu, L. Klein, S. GÜNNEMANN, and F. Noé, "Consistent sampling and simulation: Molecular dynamics with energy-based diffusion models," (2025).
- ³⁶P. C. T. Souza, R. Alessandri, J. Barnoud, S. Thallmair, I. Faustino, F. Grünewald, I. Patmanidis, H. Abdizadeh, B. M. H. Bruininks, T. A. Wassenaar, P. C. Kroon, J. Melcr, V. Nieto, V. Corradi, H. M. Khan, J. Dománski, M. Javanainen, H. Martinez-Seara, N. Reuter, R. B. Best, I. Vattulainen, L. Monticelli, X. Periole, D. P. Tieleman, A. H. de Vries, and S. J. Marrink, "Martini 3: a general purpose force field for coarse-grained molecular dynamics," *Nat. Method* **18**, 382–388 (2021).
- ³⁷T. Bereau, L. J. Walter, and J. F. Rudzinski, "Martignac: Computational workflows for reproducible, traceable, and composable coarse-grained martini simulations," *J. Chem. Inf. Model.* **64**, 9413–9423 (2024).
- ³⁸H. J. Berendsen, D. van der Spoel, and R. van Drunen, "Gromacs: A message-passing parallel molecular dynamics implementation," *Comput. Phys. Commun.* **91**, 43–56 (1995).
- ³⁹G. Bussi, D. Donadio, and M. Parrinello, "Canonical sampling through velocity rescaling," *J. Chem. Phys.* **126**, 014101 (2007).
- ⁴⁰M. Bernetti and G. Bussi, "Pressure control using stochastic cell rescaling," *J. Chem. Phys.* **153**, 114107 (2020).
- ⁴¹T. P. consortium, "Promoting transparency and reproducibility in enhanced molecular simulations," *Nature Methods* **16**, 670–673 (2019).
- ⁴²K. Vanommeslaeghe, E. Hatcher, C. Acharya, S. Kundu, S. Zhong, J. Shim, E. Darian, O. Guvench, P. Lopes, I. Vorobyov, and A. D. MacKerell, "Charmm general force field: A force field for drug-like molecules compatible with the charmm all-atom additive biological force fields," *J. Comput. Chem.* **31**, 671–690 (2009).
- ⁴³J. B. Klauda, R. M. Venable, J. A. Freites, J. W. O'Connor, D. J. Tobias, C. Mondragon-Ramirez, I. Vorobyov, A. D. MacKerell, and R. W. Pastor, "Update of the charmm all-atom additive force field for lipids: Validation on six lipid types," *J. Phys. Chem. B* **114**, 7830–7843 (2010).
- ⁴⁴S. Jo, T. Kim, V. G. Iyer, and W. Im, "Charmm-gui: A web-based graphical user interface for charmm," *J. Comput. Chem.* **29**, 1859–1865 (2008).
- ⁴⁵S. Feng, S. Park, Y. K. Choi, and W. Im, "Charmm-gui membrane builder: Past, current, and future developments and applications," *J. Chem. Theory Comput.* **19**, 2161–2185 (2023).
- ⁴⁶J. Lee, X. Cheng, J. M. Swails, M. S. Yeom, P. K. Eastman, J. A. Lemkul, S. Wei, J. Buckner, J. C. Jeong, Y. Qi, S. Jo, V. S. Pande, D. A. Case, C. L. Brooks, A. D. MacKerell, J. B. Klauda, and W. Im, "Charmm-gui input generator for namd, gromacs, amber, openmm, and charmm/openmm simulations using the charmm36 additive force field," *J. Chem. Theory Comput.* **12**, 405–413 (2015).
- ⁴⁷K. Lindorff-Larsen, S. Piana, K. Palmo, P. Maragakis, J. L. Klepeis, R. O. Dror, and D. E. Shaw, "Improved side-chain torsion potentials for the amber ff99sb protein force field," *Proteins: Structure, Function, and Bioinformatics* **78**, 1950–1958 (2010).
- ⁴⁸J. Bradbury, R. Frostig, P. Hawkins, M. J. Johnson, C. Leary, D. Maclaurin, G. Necula, A. Paszke, J. VanderPlas, S. Wanderman-Milne, and Q. Zhang, "JAX: composable transformations of Python+NumPy programs," (2018).
- ⁴⁹J. Heek, A. Levskaya, A. Oliver, M. Ritter, B. Rondepierre, A. Steiner, and M. van Zee, "Flax: A neural network library and ecosystem for JAX," (2024), accessed: 2025-09-26.
- ⁵⁰DeepMind, I. Babuschkin, K. Baumli, A. Bell, S. Bhupatiraju, J. Bruce, P. Buchlovsky, D. Budden, T. Cai, A. Clark, I. Danihelka, A. Dedieu, C. Fantacci, J. Godwin, C. Jones, R. Hemsley, T. Hennigan, M. Hessel, S. Hou, S. Kapturowski, T. Keck, I. Kemaev, M. King, M. Kunesch, L. Martens, H. Merzic, V. Mikulik, T. Norman, G. Papamakarios, J. Quan, R. Ring, F. Ruiz, A. Sanchez, L. Sartran, R. Schneider, E. Sezener, S. Spencer, S. Srinivasan, M. Stanojević, W. Stokowiec, L. Wang, G. Zhou, and F. Viola, "The DeepMind JAX Ecosystem," (2020), accessed: 2025-09-26.
- ⁵¹I. Loshchilov and F. Hutter, "Decoupled weight decay regularization," arXiv cs.LG (2017), 10.48550/arXiv.1711.05101.
- ⁵²P. Ramachandran, B. Zoph, and Q. V. Le, "Searching for activation functions," arXiv cs.NE (2017), 10.48550/arXiv.1710.05941.
- ⁵³J. Comer, K. Schulten, and C. Chipot, "Diffusive models of membrane permeation with explicit orientational freedom," *J. Chem. Theory Comput.* **10**, 2710–2718 (2014).
- ⁵⁴M. Ghorbani, E. Wang, A. Krämer, and J. B. Klauda, "Molecular dynamics simulations of ethanol permeation through single and double-lipid bilayers," *J. Chem. Phys.* **153** (2020), 10.1063/5.0013430.
- ⁵⁵C. H. Tse, J. Comer, S. K. Sang Chu, Y. Wang, and C. Chipot, "Affordable membrane permeability calculations: Permeation of short-chain alcohols through pure-lipid bilayers and a mammalian cell membrane," *J. Chem. Theory Comput.* **15**, 2913–2924 (2019).
- ⁵⁶A. Krämer, A. Ghysels, E. Wang, R. M. Venable, J. B. Klauda, B. R. Brooks, and R. W. Pastor, "Membrane permeability of small molecules from unbiased molecular dynamics simulations," *J. Chem. Phys.* **153** (2020), 10.1063/5.0013429.